

# Particle image velocimetry and visualization of natural and forced flow around rectangular cylinders

By RICHARD MILLS, JOHN SHERIDAN  
AND KERRY HOURIGAN†

Fluids Laboratory for Aeronautical and Industrial Research (FLAIR), Department of Mechanical Engineering, Monash University 3800, Australia

(Received 18 March 2002 and in revised form 7 October 2002)

Particle image velocimetry (PIV) measurements and flow visualization in a water tunnel show that vortex shedding at the leading and trailing edges of rectangular cylinders can be simultaneously phase-locked to transverse velocity perturbations when the applied perturbation  $St_p$  is close to an impinging leading-edge vortex/trailing-edge vortex shedding (ILEV/TEVS) frequency. The transverse perturbations, analogous to  $\beta$ -mode duct acoustic resonances, are generated through harmonic oscillations of the sidewalls. When this occurs, the leading-edge vortices are found always to pass the trailing edge at the same phase in the perturbation cycle regardless of the chord-to-thickness ( $c/t$ ) ratio. Applying perturbations at an  $St_p$  not equal to the natural global frequency also results in phase-locked vortex shedding from the leading edge, and a near wake with a frequency equal to the perturbation frequency. This is consistent with previous experimental findings. However, vortex shedding at the trailing edge is either weaker or non-existent. PIV results and flow visualization showed trailing-edge vortex growth was weaker because leading-edge vortices arrive at the trailing edge at a phase in the perturbation cycle where they interfere with trailing-edge shedding. The frequencies at which trailing-edge vortices form for different  $c/t$  ratios correspond to the natural ILEV/TEVS frequencies. As in the case of natural shedding, peaks in base suction occur when the leading-edge vortices pass the trailing edge at the phase in the perturbation cycle (and thus in the leading-edge shedding cycle) that allows strong trailing-edge shedding. This is the reason for the similarity in the  $St$  vs.  $c/t$  relationship for three seemingly different sets of experiments.

---

## 1. Introduction

The impinging shear-layer instability mechanism was proposed by Nakamura & Nakashima (1986) to explain vortex formation from elongated bluff bodies, and thus the stepwise variations of  $St_c$  with the ratio,  $c/t$ , of chord,  $c$ , to thickness,  $t$ . Naudascher & Rockwell (1994) more accurately called this the impinging leading-edge vortex (ILEV) instability mechanism, since for long plates ( $c/t > 7$ ), it is vortices shed from the leading-edge separation bubble that interact with the trailing edge rather than the leading-edge shear layer doing so directly. The ILEV instability mechanism originally arose from work reviewed by Rockwell & Naudascher (1978) that focused

† Author to whom correspondence should be addressed: kerry.hourigan@eng.monash.edu.au

on the mechanism(s) controlling self-sustained oscillations of flow over a sharp-edged cavity. Rockwell & Naudascher described three categories of self-sustained fluid oscillations:

(i) Fluid dynamic oscillations, where the instability of the cavity shear layer is enhanced by a feedback mechanism originating at the downstream corner of the cavity. The acoustic feedback wavelength is much larger than the cavity length, so the process can be considered to be hydrodynamic.

(ii) Fluid resonant oscillations, which are strongly coupled with resonant wave effects within the cavity. The acoustic wavelength is of the same order of magnitude as the cavity size.

(iii) Fluid-elastic oscillations that result from the periodic displacements of one or more of the cavity walls exerting feedback control on the separating shear layer.

For all three types of self-sustained fluid oscillation defined by Rockwell & Naudascher, there is some sort of feedback control on the convectively unstable leading-edge separating shear layer. Ho & Nosseir (1981) studied the feedback mechanism of a free jet impinging on a large flat plate mounted normal to the jet. They found that the feedback loop controlling vortex formation in the free shear layers of the jet had two fundamental components:

(i) Large-scale coherent vortex structures propagating downstream.

(ii) Upstream propagating pressure waves that travel at the speed of sound, generated by the impingement of the large-scale coherent structures on the plate surface.

The upstream propagating pressure waves force the separating shear layer originating at the jet exit at a subharmonic of its 'intrinsic most unstable frequency', which results in a vortex amalgamation process that was observed by Ho & Huang (1982) in experiments on a mixing layer. The vortex amalgamation completes the feedback loop, and is responsible for the generation of the large-scale structures that impinge on the flat plate at intervals that are phase-locked with the upstream propagating pressure waves. In the present paper, the sidewalls of a water tunnel are oscillated to over-ride the feedback pressure waves and force the flow around rectangular plates over a range of frequencies.

The ILEV instability mechanism is a fluid resonant oscillation. The shear-layer instability is greatly enhanced by the feedback control of the trailing-edge discontinuity on the vorticity production at the separation point. Regular and periodic shedding of vortices (hereinafter referred to as L vortices) occurs at the leading-edge. As an L vortex, shed during an earlier shedding cycle, passes the trailing edge, a pressure pulse is generated and travels upstream to the receptive leading-edge shear layer on the same side of the plate. This causes the L vortex that was forming at the leading edge on the same side to be shed, and a new L vortex to begin forming. In this manner, the wavelength of vortex shedding is locked to the plate chord. Plates with  $c/t$  between 3 and 5 have just one L vortex on each side, and thus shed vortices at ILEV mode  $n = 1$ . As  $c/t$  is increased from 3 to 5, the wavelength of these L vortices increases until a limit is reached, and the shedding jumps to the next ILEV mode ( $n = 2$ ).

Nakamura & Nakashima (1986) found from their work on the H section prisms that a plate with  $c/t = 5$  shed vortices from the leading edge at the same frequency with and without a splitter plate placed behind the trailing edge of the model. This indicates that the ILEV instability mechanism is one-sided. Unlike vortex shedding from short bluff bodies, it is not dependent on the interaction of the two separated shear layers in the wake. It is worth noting that the Reynolds number,  $Re$ , for the H section prisms studied was 50 000 or higher (based on the plate thickness,  $t$ ), and the

frequency spectrum of hot-wire measurements made in the wake showed no sharp spectral peaks for plates with  $c/t > 8$ . This is consistent with the findings of Parker & Welsh (1983) for flow over rectangular plates at similar  $Re$ , where it was found that for rectangular plates with  $c/t > 7.6$ , no sharp spectral peaks were observed in the wake.

The study by Nakamura, Ohya & Tsuruta (1991) on flows around rectangular plates found that the ILEV instability was present for plates with  $c/t$  up to 16. However, for plates with  $c/t > 6$ , Nakamura could not detect any regular vortex shedding for  $Re > 2000$ . For low  $Re$ , the shear layer separating from the leading-edge corners is initially laminar, and remains so for up to approximately one plate thickness away from the leading edge. As  $Re$  is increased, Kelvin–Helmholtz vortices appear in the separated shear layers as the transition point moves further upstream, making the shear layer less sensitive to external disturbances. Also, the flow along the plate sides becomes increasingly three-dimensional as  $Re$  increases. These two factors would be expected to combine to weaken the effect of any feedback mechanism for  $Re > 2000$ .

There are three possible classes of vortex shedding regimes for stationary rectangular cylinders characterized by Naudascher & Rockwell (1994): Class I, leading-edge vortex shedding (LEVS); Class II, impinging leading-edge vortices (ILEV); and Class III, trailing-edge vortex shedding (TEVS).

Regular shedding was observed by Stokes & Welsh (1986) from a rectangular plate in a duct at high  $Re$ . Nakamura *et al.* (1991) suggested that this was a result of the ILEV instability being excited by the loud acoustic resonance set up at a duct  $\beta$ -mode (Parker 1967) resonant frequency. Stokes & Welsh (1986) demonstrated that when the acoustic resonance was excited, the source of the sound was located at the trailing edge of the rectangular plates. The sound was reflected off the walls of the duct, before interacting with the separated shear layers to lock the vortex shedding to the duct  $\beta$ -mode resonant frequency. This would appear to be an example of a category (ii) type of self-sustained oscillation defined by Rockwell & Naudascher (1978), and not arising from an ILEV instability mechanism proposed by Nakamura *et al.* (1991). Nevertheless, there is a distinct similarity between the acoustic Strouhal number at which peaks in the resonant sound pressure level occur for different length plates in the experiments of Stokes & Welsh (1986) and the ILEV shedding frequencies measured by Nakamura *et al.* (1991). The excitation of acoustic resonant modes due to vortex shedding in ducted and cavity flows has been explained in terms of Howe's (1975) aeroacoustic theory by Hourigan *et al.* (1990, 1992, 1993*b*) and Stoneman *et al.* (1988). However, to date, the contradiction between Stokes & Welsh (1986) and Nakamura *et al.* (1991) regarding the feedback mechanism controlling the vortex shedding from a plate in a duct in the presence of a resonant sound field has not been resolved.

To explain the stepwise frequency observed in shedding around rectangular plates, Hourigan *et al.* (1993*a*) introduced the vortex interaction hypothesis. Building on this hypothesis, Hourigan, Thompson & Tan (2001) investigated in more detail the role of the trailing-edge (T) vortices and found that they shed at a preferred frequency, similar to the case of an aerodynamic leading-edge plate where leading-edge shedding was absent. The feature of the flow that had not been included previously in an explanation of the feedback loop was the shedding of vortices from the trailing edge of the plates. As an L vortex approaches the trailing edge, the reattached boundary layer in front of it separates again at the trailing edge and rolls up to form a T vortex of like sign. The T vortex then interacts with the approaching L vortex from the same side of the plate, and they are shed as a pair in the wake downstream.

This interaction between L and T vortices occurs alternately on each side of the plate at the upper and lower trailing-edge corners, and results in the formation of a regular vortex street. In the natural shedding case, trailing-edge shedding at the preferred frequency was not possible at certain plate chord-to-thickness ratios and flow velocities because of interference from the L vortices; in these cases, the flow selected a nearby frequency for which trailing-edge shedding could occur. Analysis of the instantaneous pressure field led Hourigan *et al.* (2001) to the conclusion that the T vortices produced a stronger pressure pulse emanating from the trailing edge than did the L vortices. The ILEV mechanism was not really operating directly in this case; rather it was a combination of ILEV and trailing-edge vortex shedding (TEVS) that characterized the global instability leading to the observed stepwise frequency.

As well as elongated rectangular, H and T sections, Nakamura (1996) found that vortex shedding from a variety of bluff-body shapes with extended splitter plates was characterized by the ILEV instability. Consistent with earlier results, the ILEV instability for flow around a circular cylinder with a splitter plate could only sustain shedding of the  $n=1$  mode at  $Re=5000$  based on cylinder diameter, but the  $n=2$  mode was observed at  $Re=1600$ . Another example of the ILEV instability was investigated by Nguyen (1990). He found that transverse vibrations of gates used to control open channel flows excited vortex shedding corresponding to ILEV modes 1 and 2.

The study by Mills, Sheridan & Hourigan (2002) showed that if the flow around a rectangular cylinder in an open jet wind tunnel is forced by small transverse oscillations, similar in form to a duct resonant acoustic cross-mode, a stepwise variation in the frequency at which peak base drag occurs is found as the chord to thickness ratio of the cylinder is varied. It was postulated that in the natural shedding case, the global oscillation frequency was selected on the basis of providing the peak base drag (as this generates the dominant pressure pulse in the feedback loop back to the receptive leading-edge shear layer). By varying the forcing frequency, it was shown that indeed the maximum base drag occurred for frequencies corresponding to the natural shedding case. To strengthen the argument in favour of the vortex interaction hypothesis adopted in that paper, it must now to be established that vortex shedding at the trailing edge can be simultaneously locked to the transverse velocity perturbations with the leading-edge vortex shedding. The aim of the current study is to provide detailed particle image velocimetry (PIV) imaging and flow visualization of flow around rectangular plates performed in a water tunnel to show that this simultaneous locking occurs. Furthermore, it will be shown that significant interference of the trailing-edge shedding by the leading-edge vortices depends on the phase in the shedding cycle at which the leading-edge vortices arrive at the trailing edge; indeed, suppression of the trailing-edge vortex shedding can occur at some forcing frequencies.

## 2. Experimental method

### 2.1. Water tunnel

#### 2.1.1. Tunnel design

The low-turbulence closed-circuit water tunnel used was designed and constructed at the CSIRO, Melbourne. A diagram of the water tunnel and working section is shown in figure 1. A pump driven by an a.c. electric motor was used to generate the mean flow in the tunnel test section. Water was pumped through a diffuser

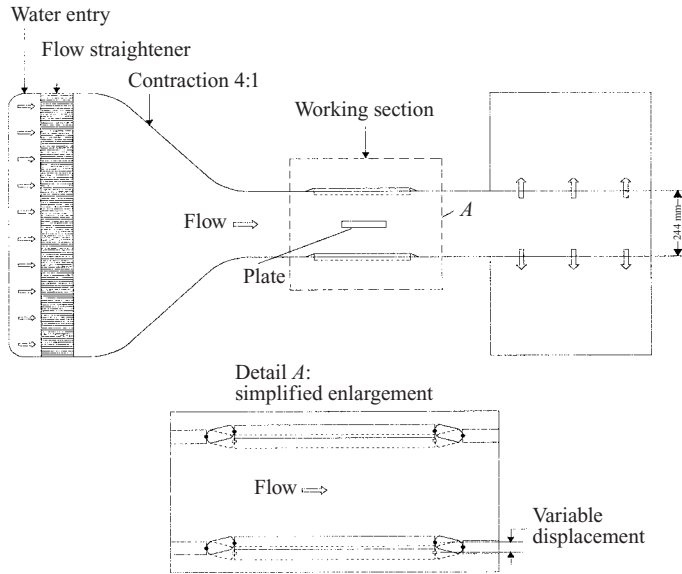


FIGURE 1. Schematic of the water tunnel working section.

incorporating screens into a settling chamber containing filter material, and a honeycomb section. The water then passed through a two-dimensional four-to-one contraction with an outlet dimension of  $244 \text{ mm} \times 244 \text{ mm}$  into a duct of the same cross-section. There were three sections of the duct, all constructed of 20 mm thick clear acrylic sheet. The first section was 660 mm long followed by the working section, which was 770 mm long, and then a 440 mm long section, which was connected to an outlet reservoir.

The working section had flexibly mounted sidewalls to allow a velocity perturbation to be applied in a direction perpendicular to the mean flow. The applied velocity perturbation was similar to that imposed by a resonant acoustic  $\beta$ -mode (Parker 1966, 1997). The two 400 mm long movable sidewalls had glass windows, and were rigidly connected to each other and sealed to the remainder of the test section by a thin flexible membrane. Harmonic oscillations of the sidewalls were produced by a variable-speed drive. The drive was connected to the sidewall support frame via a crank and connecting rod, which allowed a variable stroke. The oscillation amplitude of the sidewalls could be varied from 0 to 5 mm at frequencies between 0 and 6 Hz. A Schlumberger DG5 linear displacement transducer was used to monitor the oscillating test section wall displacements, the output of which was recorded by the computer via an A/D board.

For a typical output from the linear displacement transducer taken with the sidewalls oscillating at a frequency of 0.75 Hz and an amplitude of 0.4 mm, a fast Fourier transform of the signal showed a spectral peak at the sidewall oscillation frequency, with the harmonics being at least 25 dB lower.

With the perturbations being periodic in nature, the phase of the perturbation cycle is defined relative to the perturbation velocity field, as shown in figure 2. Assuming the perturbations are sinusoidal with angular frequency,  $\omega$ , the perturbation velocity at any time ( $\tau$ ) is given by the function  $u(\tau) = u' \sin(\omega\tau)$ , where the phase of the perturbation cycle at any time is equal to  $\omega\tau$ . Thus, a perturbation phase angle of  $0^\circ$

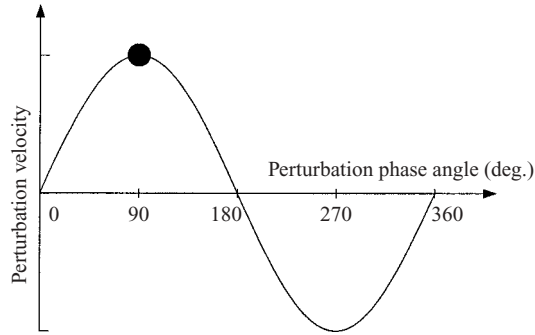


FIGURE 2. Graph of perturbation velocity *vs.* perturbation phase angle.

denotes a zero perturbation velocity but about to increase in the upwards direction, whereas  $90^\circ$  denotes the maximum perturbation velocity in the upwards direction.

### 2.1.2. Tunnel characteristics

The speed of the motor driving the pump was accurately controlled by a Danfoss a.c. 3-phase motor controller. The velocity ( $U_\infty$ ) in the working section could be varied between  $0 \text{ m s}^{-1}$  and  $0.4 \text{ m s}^{-1}$ , and the mean velocity variation, measured with a hot film and with PIV measurements, was less than  $\pm 0.5\%$  of  $U_\infty$  across the test section. For the velocities used in the experiments, the mean longitudinal turbulence level was approximately  $0.1\%$  of  $U_\infty$  at the tunnel speed of  $0.1 \text{ m s}^{-1}$  when band-pass filtered between  $0.08 \text{ Hz}$  and  $20 \text{ Hz}$ . No distinct spectral peaks were observable in the natural turbulence spectrum within this frequency range. A full description of the tunnel characteristics is given by Wu *et al.* (1993).

### 2.1.3. Water tunnel models

Test plates were made from clear acrylic; all plates used spanned the  $244 \text{ mm}$  wide working section of the water tunnel. Five plates with rectangular cross-sections were constructed with  $c/t$  ratios ranging from 6 to 10 in integer steps. They were all constructed from the same sheet of acrylic, and each had a nominal thickness of  $11.8 \text{ mm}$  ( $\pm 0.1 \text{ mm}$ ). Using these models avoided having to change the tunnel speed in order to maintain the  $Re$  constant, and allowed the same relative velocity perturbation level to be applied easily to each model without changing the amplitude of the sidewall oscillation.

All models were located vertically on the centreline of the working section, as shown in figure 1. The  $Re$  for the PIV measurements was 490, based on plate thickness. The water temperature was approximately constant at  $15^\circ\text{C}$  for all experiments.

## 2.2. Particle image velocimetry (PIV)

Using the PIV technique, instantaneous velocities of a fluid can be measured over a region illuminated by a two-dimensional sheet of light. The film-based high image density PIV technique used will be described in this section. Adrian (1991), and more recently Grant (1997), reviewed the concept of high image density PIV, and the technique is now widely accepted as a reliable method of obtaining instantaneous velocity data for flows around bluff bodies.

### 2.2.1. Flow seeding and illumination

The flow was seeded with silver-coated hollow glass particles of  $<40\ \mu\text{m}$  in diameter, and close to neutrally buoyant. With the largest particles used having a diameter of  $40\ \mu\text{m}$ , the maximum particle slip velocity was less than 0.2% of free-stream velocity.

In this system, the particles were illuminated using light from a continuous 6 W argon-ion laser. In order to obtain a PIV image, the laser light was first passed through a mechanical shutter connected to a 486 PC. The shutter could be controlled to generate laser light pulses with pulse durations of 1 ms. A  $50\ \mu\text{m}$  diameter multi-mode optical fibre cable was used to transmit the light, which was spread into a thin sheet using a cylindrical lens, and passed through a sidewall of the working section. The thickness of the laser sheet was adjusted to 1 mm by varying the spacing between the two lenses at the outlet of the fibre optics.

For all PIV images processed, 3 light pulses were used. This reduced the chance of false detection of pairs compared to using 2 pulses, both when automatically processing the image using the autocorrelation technique, and when manually editing regions of the flow where vectors were not resolved automatically. To be able to obtain a velocity vector from each interrogation window, particle concentrations of 3–10 particles were considered adequate for each interrogation window (Wu 1994).

### 2.2.2. Image acquisition

A 35 mm Nikon F90X single lens reflex camera was used to record PIV images onto Kodak Tmax 400 black and white film. The camera shutter was triggered by the 486 PC, using a Nikon remote triggering lead connected to the parallel port of the PC. The PC was used to control the timing of camera triggering and laser pulsing to coincide with the velocity bias mirror being at the midpoint of its oscillation cycle.

For this film-based PIV system, the digital film scanner was a limiting factor on the resolution of the PIV images, as the film resolution was an order of magnitude higher than that of the scanner. The resolution of the scanner was  $106.3\ \text{pixels}\ \text{mm}^{-1}$ , giving the resolution of a digitized 35 mm frame as approximately  $3543 \times 2657$  pixels. In order to minimize the number of false or unresolved vectors produced by the autocorrelation, a minimum intensity threshold level of the digitized image was adjusted to remove background noise.

### 2.2.3. Bias velocity mirror

To enable an autocorrelation technique to be used on reversing flows, a  $50\ \text{mm} \times 50\ \text{mm}$  plane mirror was used to reflect the image from the working section towards the camera. The mirror was mounted on the shaft of a General Scanning G325DT scanner, which was used to rotate the mirror at a constant angular velocity. The axis of rotation of the mirror was parallel with the sheet of laser light, and perpendicular to the mean flow direction. This allowed a bias velocity to be added to the image in the direction of the mean flow ( $U_\infty$  direction) so that all  $U$  velocity components would be positive. For the flows photographed, a bias velocity approximately equal to the free-stream velocity allowed PIV data to be resolved without any ambiguity over the entire image frame. After obtaining a velocity vector field from the image, the bias velocity was then subtracted from the original velocity field to obtain the velocity field in the laboratory reference frame.

### 2.2.4. Image processing

Once digitized, individual PIV images were processed on a Silicon Graphics workstation using the program PIVFlow written by N. Lawson at the CSIRO.

PIVFlow uses an auto-correlation technique to extract a grid of velocity vectors from the PIV image. Using the software PIVFlow, an interrogation window size of  $64 \times 64$  pixels was found to be satisfactory. The number of gridpoints used was  $110 \times 45$ , which gave an overlap ratio of at least 50% between adjacent interrogation windows.

The spatial autocorrelation function,

$$R_{xx}(r_d) = \int I(r)I(r + r_d) dr, \quad (1)$$

of the transmitted light intensity ( $I$ ) can be found by taking a Fourier transform of the fringe pattern produced by coherent illumination of a PIV image. The variable  $r$  is the position in the film plane and  $r_d$  is the displacement vector between members of an image pair. To avoid obtaining a vector field with entirely zero vectors owing to the self-correlation peak at the origin of each interrogation window, a d.c. mask with a radius set equal to the radius (in pixels) of the largest particle was used. The autocorrelation peaks measured were then due to the two peaks at displacements of plus and minus the displacements between particle images.

### 2.2.5. Post processing

The PIVFlow program also facilitated post-processing of the PIV data, by removing any false vectors, and by smoothing noise generated by the autocorrelation technique. A range of acceptable velocities for each image could be set to remove false vectors outside this range automatically. Individual grid points could also be manually edited to correct unresolved or false velocity vectors that fell within the acceptable velocity range. In regions where there were no data, velocity vectors could be calculated using a linear interpolation between surrounding grid points.

To overcome the random noise associated with digital image processing, spatial filtering techniques are frequently used. The PIVFlow program uses a low-pass Gaussian filter to smooth the PIV data after processing. For the images processed, smoothing the data using the low-pass Gaussian filter over a radius of 2 produced the best results. The only regions of the flow where this choice of smoothing radius was not appropriate were those gridpoints immediately adjacent to the bluff body, where high values of peak vorticity associated with the thin boundary layer were lost owing to smoothing. This gave the appearance of a thicker boundary layer than was actually the case.

The vorticity at grid points was found numerically from the discrete velocity data using a central difference scheme.

### 2.2.6. Flow visualization

Flow visualization was performed in the water tunnel with the same hardware used to obtain the PIV images. Typically, the laser was pulsed 10 times with pulses of 2 ms in duration to obtain particle streaklines of suitable length. The bias velocity mirror was used to physically remove the mean flow velocity component, effectively placing the camera in a reference frame moving at the convection rate of the vortices. This was useful in revealing vortex structures in the flow.

## 3. Results and discussion

PIV experiments and flow visualization were performed on rectangular plates, with  $c/t$  varying between 6 and 10, in the water tunnel. All PIV measurements

on rectangular plates were performed with  $Re = 490$ , where the flow remains largely two-dimensional even in the absence of transverse velocity perturbations. It was not possible to perform these experiments at the same  $Re$  used in the wind-tunnel experiments, because of the limitations of the PIV system at higher velocities. Although the shear layer is laminar at  $Re = 490$  and the vortex structures shed from the leading edge are largely two-dimensional, performing experiments at this low  $Re$  is justified because the effect of the transverse velocity perturbations used in the higher  $Re$  wind-tunnel experiments is to suppress the downstream development of three-dimensionality in the flow. Thus, when the higher  $Re$  flow is phase-locked to transverse velocity perturbations, it can be considered to be quasi-two-dimensional, consisting of regularly spaced spanwise vortices with an associated secondary three-dimensional random component (Hourigan *et al.* 1993a).

### 3.1. Natural vortex shedding (no perturbations applied)

Performing experiments at low  $Re$  also allowed a direct comparison to be made with the results of Nakamura *et al.* (1991) and Ohya *et al.* (1992), which were from experiments performed at  $Re = 1000$ . For  $Re < 2000$  and in the absence of external flow disturbances, a feedback mechanism involving the ILEV instability and the TEVS characterizes vortex shedding from long rectangular plates (Hourigan *et al.* 2001; Mills *et al.* 2002).

PIV results are shown in figure 3 for a rectangular plate with  $c/t = 6$ . The velocity vector plot (figure 3a) and the sectional streamline plot (figure 3b), both in a stationary reference frame, show the existence of a clockwise rotating vortex forming at the trailing edge of the model (T vortex). The choice of reference frame significantly affects the form of the flow structures that can be observed when looking at either velocity vector plots or streamline plots (Perry, Chong & Lim 1982). This is clear when viewing the velocity vector plot (figure 3c) and the sectional streamline plot (figure 3d), both in a reference frame moving at the convection velocity of the wake vortices ( $U_{conv} = 0.75U_\infty$ ), where the clockwise T vortex is not revealed. Also, a clockwise rotating L vortex on the upper side of the plate adjacent to the trailing edge can clearly be seen, whereas this was not obvious in figures 3(a) and 3(b). However, the vorticity plot (figure 3e) clearly shows both clockwise rotating L and T vortices near the upper trailing-edge corner, as well as other vortices in the flow since vorticity is Galilean invariant and hence is not affected by the choice of reference frame. The vorticity concentrations in the wake result from the merging of L and T vortices of like sign at the trailing edge before being shed into the wake.

Further evidence of the simultaneous shedding of L and T vortices can be seen in the flow visualizations in figure 4. As with the velocity vector plots and streamline plots, the choice of reference frame can greatly alter the interpretation of a flow visualization image. Figure 4(a) (in a fixed reference frame) clearly shows the formation of a clockwise rotating vortex at the trailing edge, while figure 4(b) (in a reference frame moving with the vortices) shows the presence of only a clockwise rotating L vortex adjacent to the trailing edge. For this reason, only vorticity plots, arising from the PIV experiments, are shown in the remainder of this paper.

Vorticity contour plots are presented in figure 5, showing the existence of both L and T vortices in the flow around longer rectangular plates with  $c/t$  ratios of 7, 8, 9 and 10. This confirms the computational fluid dynamics results of Ohya *et al.* (1992), Tan, Thompson & Hourigan (1998) and Hourigan *et al.* (2001), which showed the shedding of both L and T vortices to be a feature of natural vortex shedding from elongated rectangular plates.

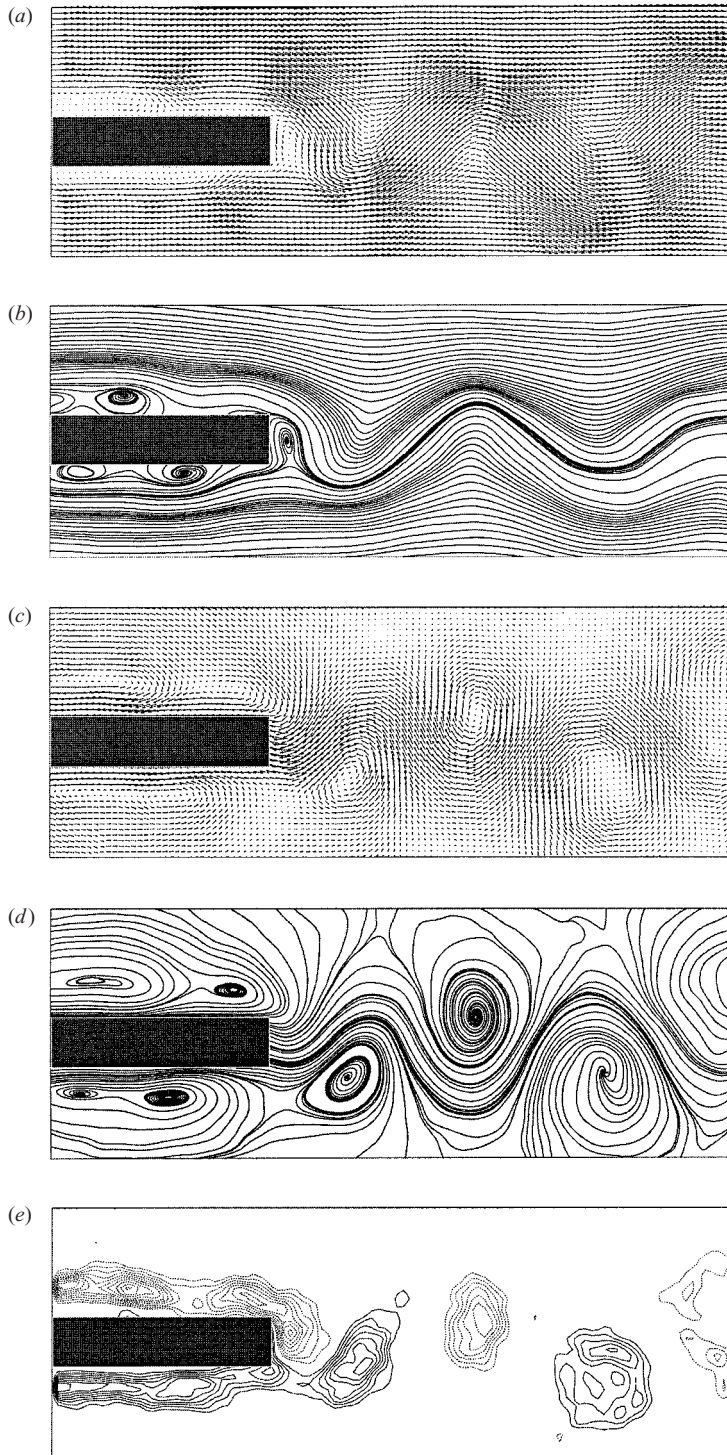


FIGURE 3. PIV results for flow past the trailing edge of a rectangular plate with  $c/t = 6$ , at  $Re = 490$ . (a) Velocity vector plot (laboratory reference frame). (b) Sectional streamline plot (laboratory reference frame). (c) Velocity vector plot (reference frame moving at  $0.75U_\infty$  in the direction of the flow). (d) Sectional streamline plot (reference frame moving at  $0.75U_\infty$ ). (e) Vorticity contour plot.

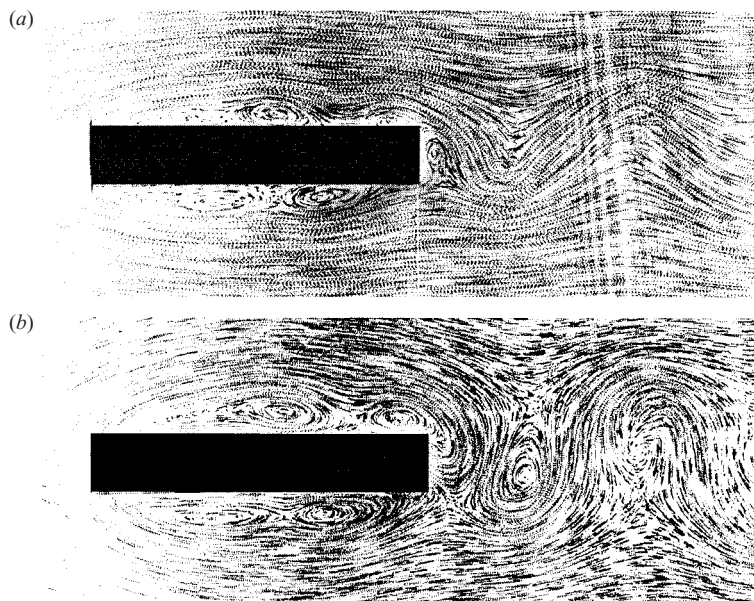


FIGURE 4. Visualization of flow about a rectangular plate with  $c/t = 6$ , at  $Re = 490$ . (a) Stationary reference frame. (b) Reference frame moving with the vortices in the wake (using the bias velocity mirror).

Figure 6 shows the comparison between the self-sustained Strouhal numbers,  $St_c$ , based on the chord for all the rectangular plates tested in the water tunnel at  $Re = 490$  and  $St_c$  for the data presented by Nakamura *et al.* (1991) with  $Re = 1000$ . The similarity between the two sets of results indicates that the vortex-shedding frequencies associated with the ILEV/TEVS instability are not greatly affected by changes in  $Re$  over the range in which it affects vortex shedding from long rectangular plates. The only significant difference between the two sets of results is the vortex-shedding frequency for the plate with  $c/t = 9$ . Nakamura *et al.* (1991) found that this plate shed vortices at the  $n = 3$  ILEV/TEVS mode, whereas the model in the water tunnel shed vortices at the  $n = 2$  ILEV/TEVS mode.

The mechanism by which a particular ILEV/TEVS mode is selected and the importance of the trailing-edge shedding are discussed in Hourigan *et al.* (2001). One possible explanation for the disparity in the shedding frequency for the  $c/t = 9$  plate between the current results and those of Nakamura *et al.* (1991) is the difference in tunnel blockage ratio between the two sets of experiments. This would alter the convection velocity of L vortices, thus slightly affecting the spacing between them. Given the prescribed frequency of shedding, a higher convection velocity would result in a larger spacing between vortices for a given plate. The same effect on the spacing between L vortices would be observed by increasing the plate length slightly. This means that the  $c/t = 9$  plate, which shed vortices at the  $n = 2$  ILEV/TEVS mode in the water tunnel, would shed vortices at the same frequency as a slightly shorter plate in a wind tunnel with a smaller blockage ratio. Another difference between the two experiments is the  $Re$ ; it is possible that  $Re$  affects the plate  $c/t$  ratio at which vortex shedding changes from one ILEV/TEVS mode to another through, for example, changes in the mean convection velocity of vortices.

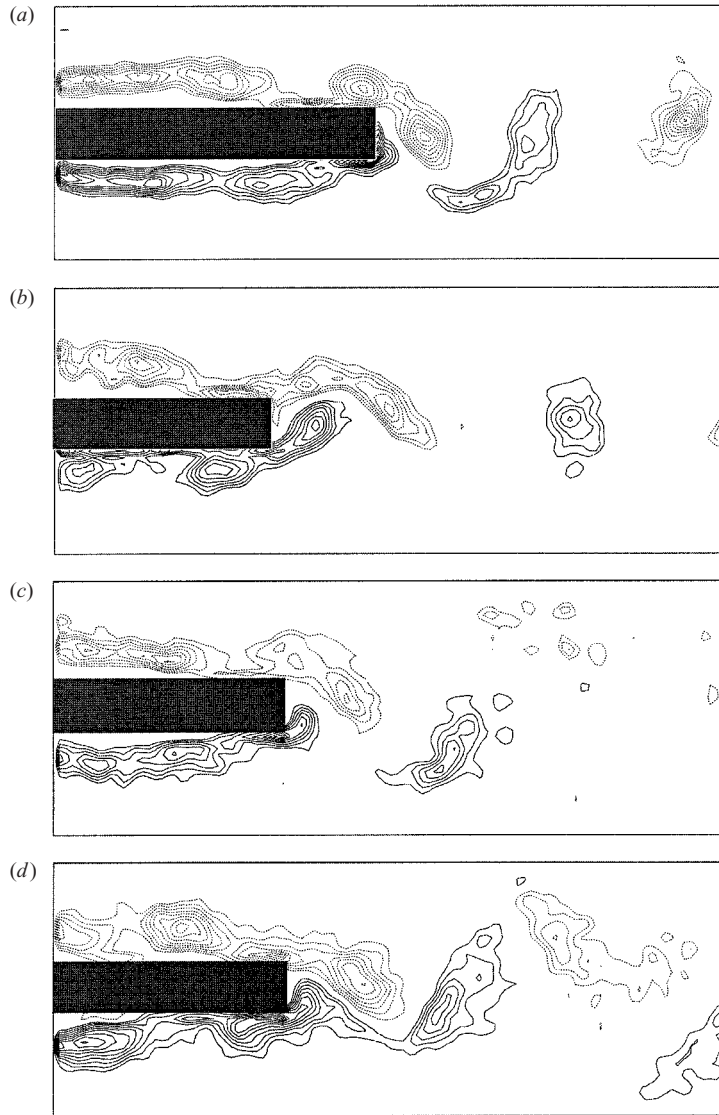


FIGURE 5. Vorticity contour plots for flow past the trailing edge of rectangular plates.  $Re = 490$ . (a)  $c/t = 7$ , (b) 8, (c) 9, (d) 10.

### 3.2. Transverse velocity perturbations applied at natural ILEV/TEVS frequencies

To test the vortex interaction hypothesis, the effect of applying transverse velocity perturbations at the natural ILEV/TEVS frequency of each rectangular plate was investigated. Figure 7(b) shows PIV images of a full shedding cycle taken of the flow about a rectangular plate with  $c/t = 6$  in the presence of a 5% velocity perturbation applied at a frequency of 0.68 Hz (or forced Strouhal number based on thickness,  $St_p = 0.192$ ). This is the natural vortex-shedding frequency for the same plate with an ILEV/TEVS mode of 2. The perturbation phase angle is  $90^\circ$  (see figure 2), meaning that the perturbation velocity is a maximum in the upwards direction. The free-stream velocity is  $41.8 \text{ mm s}^{-1}$  ( $Re = 490$ ). At this forcing of  $St_p = 0.192$ , both the

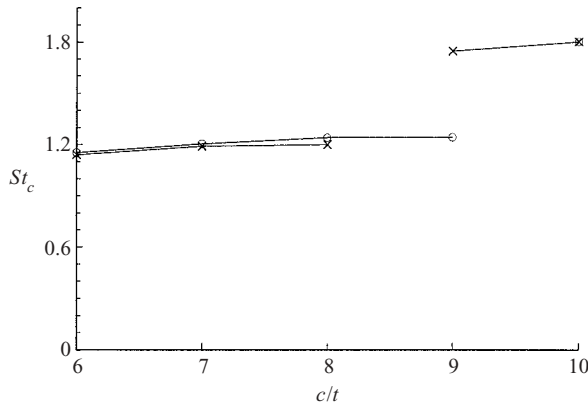


FIGURE 6. Comparison of vortex-shedding frequencies for rectangular plates with ( $6 \leq c/t \leq 10$ );  $\circ$ ,  $Re = 490$  (present experiments);  $\times$ ,  $Re = 1000$  (from Nakamura *et al.* 1991).

leading-edge and trailing-edge vortex sheddings are phase-locked to the transverse velocity perturbations. Tan *et al.* (1998) have numerically simulated this flow for a rectangular plate with  $c/t = 10$  with a 5% transverse velocity perturbation applied. Their results show a similar merging of L and T vortices at the trailing edge, for cases where the perturbation results in vortex shedding being locked at both the trailing and leading edges.

In the regions between consecutive vortices shed from the leading edge, the flow reattaches to the surface of the plate. As this reattached boundary-layer fluid is convected past the trailing edge, it rolls up to form a T vortex. At a phase angle of  $180^\circ$  (figure 7c), an anticlockwise rotating T vortex has almost completed forming from the reattached boundary-layer fluid from the lower side of the trailing-edge, while an L vortex of like sign is approaching on the lower side of the trailing edge. On the side of the plate adjacent to the upper trailing-edge corner is reattached boundary-layer fluid that is starting to form a clockwise rotating T vortex in the next half-cycle of vortex shedding. An image corresponding to a phase angle of  $270^\circ$  is shown in figure 7(d). In this image, it can be seen that the anticlockwise rotating L and T vortices near the lower side of the trailing edge are merging in the wake to become mainly a single vortex (in the wake downstream, merging of T and L vortices shed in previous half-cycles can be observed). There is a clockwise rotating T vortex forming from the reattached boundary-layer fluid from the upper side of the trailing edge, while an L vortex is approaching the upper side of the trailing edge.

Figure 8 shows four vorticity plots for a plate with  $c/t = 7$  in the presence of a 5% velocity perturbation applied at a frequency of 0.61 Hz ( $St_p = 0.172$ ). Each plot is a quarter of a perturbation cycle apart in phase. The forced frequency is equal to the natural vortex-shedding frequency for the plate with  $c/t = 7$ , corresponding to an ILEV/TEVS mode of 2.

Applying a 5% transverse velocity perturbation to the flow around a plate with  $c/t = 7$  at the same frequency as the natural vortex-shedding frequency results in vortex shedding at both the leading and trailing edges being phase-locked to the perturbations, as for the plate with  $c/t = 6$ . Comparing figure 8(b) with figure 7(b) for the plate with  $c/t = 6$ , both show an anticlockwise rotating vortex forming at the lower trailing-edge corner when the perturbation phase angle is  $90^\circ$ . This vortex

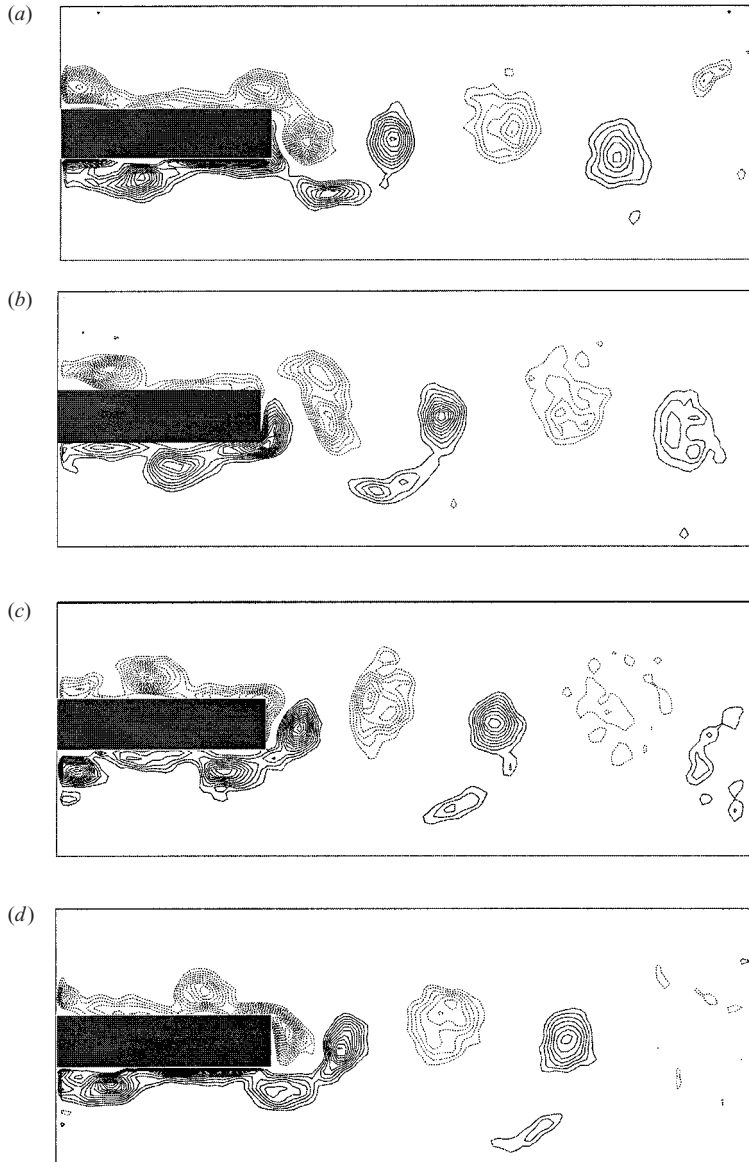


FIGURE 7. Vorticity contour plots for flow past the trailing edge of a rectangular plate with  $c/t = 6$ ,  $Re = 490$ , 5% velocity perturbation,  $St_p = 0.192$ . (a)  $\phi = 0^\circ$ , (b)  $90^\circ$ , (c)  $180^\circ$ , (d)  $270^\circ$ .

forms from the reattached boundary-layer fluid between L vortices on the lower surface of the plate. Although the perturbation frequency is different in the two cases, the difference in plate length means that the L vortices shed from the upper leading-edge corner pass the trailing edge at a phase in the perturbation cycle of approximately  $0^\circ$ , whereas L vortices on the lower side pass the trailing edge at a phase in the perturbation cycle of approximately  $180^\circ$ . The phase in the perturbation cycle at which the T vortices form appears to be the same for both plate lengths.

As for the plate with  $c/t = 6$ , T vortices merge in the near wake of the plate with  $c/t = 7$  with vortices of the same sign that were shed from the leading edge during the

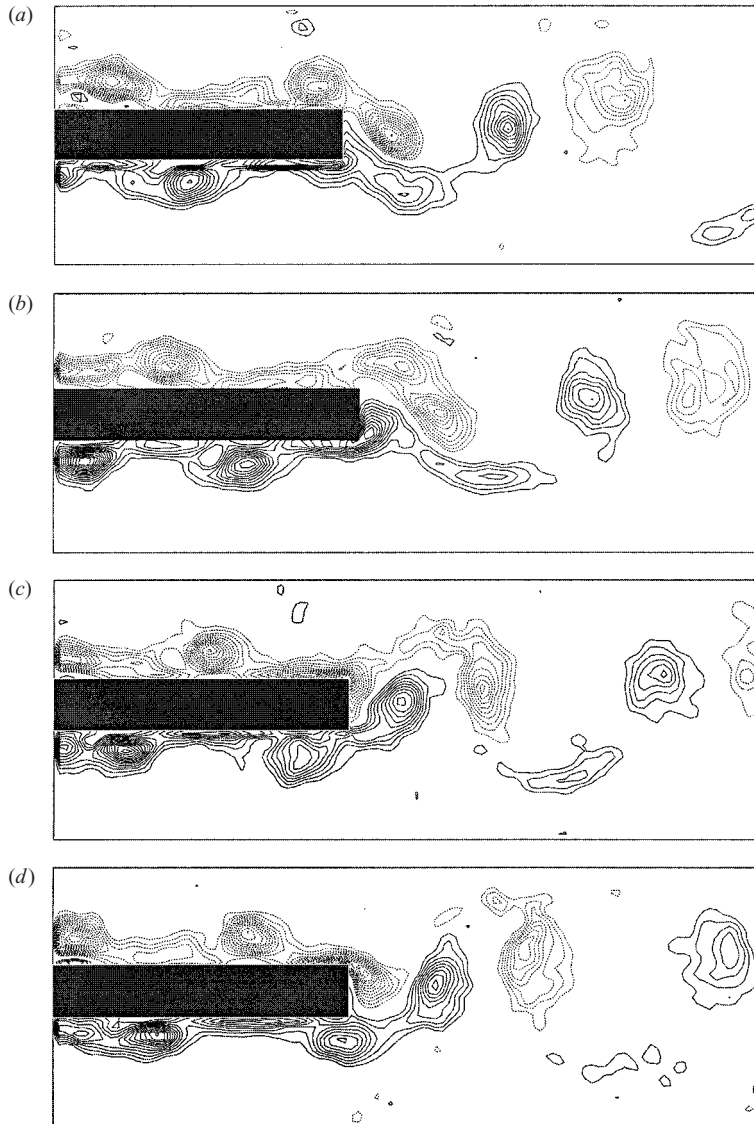


FIGURE 8. Vorticity contour plots for flow past the trailing edge of a rectangular plate with  $c/t = 7$ ,  $Re = 490$ , 5% velocity perturbation,  $St_p = 0.172$ . (a)  $\phi = 0^\circ$ , (b)  $90^\circ$ , (c)  $180^\circ$ , (d)  $270^\circ$ .

previous perturbation cycle. Also evident is some asymmetry in the vortex shedding on the upper and lower plate surfaces. Similar to the  $c/t = 6$  plate case, L vortices being convected along the upper surface of the plate are further advanced along the plate compared to L vortices on the lower surface  $180^\circ$  later in the perturbation cycle. The asymmetry in the vortex shedding is clearest when comparing the vorticity plots for the  $90^\circ$  and  $270^\circ$  phase angles in figure 7. For the plot where the phase angle is  $90^\circ$ , the clockwise L and T vortices from the upper side of the plate have almost completely merged into a single vortex. In contrast, the plot where the phase angle is  $270^\circ$  shows that the anticlockwise L and T vortices from the lower side of the plate are clearly identifiable as separate vortices. These vortices eventually merge

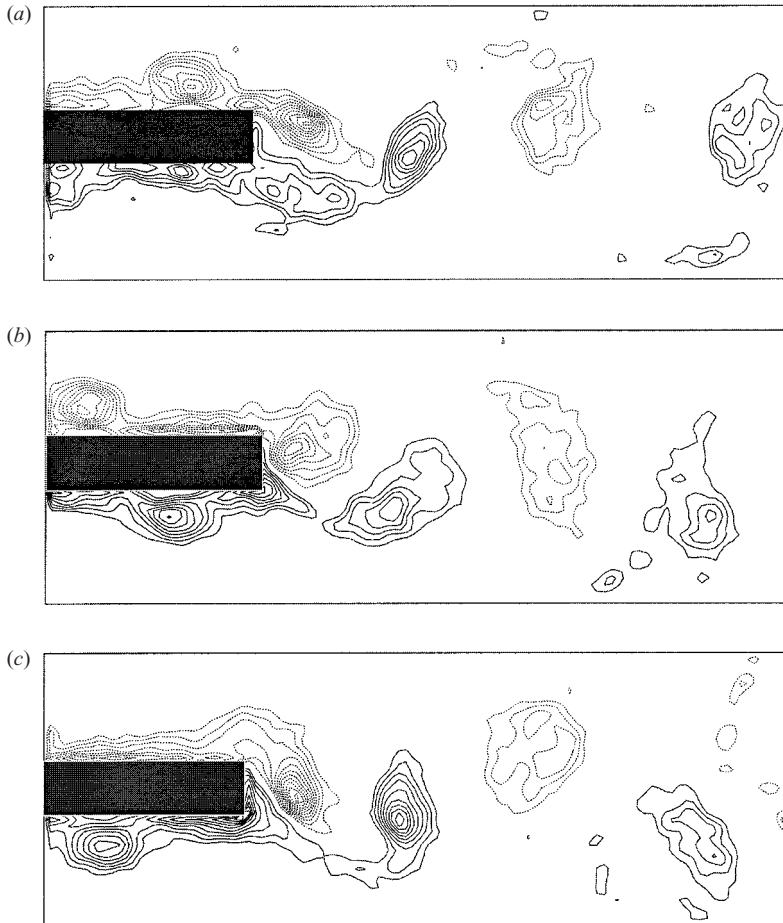


FIGURE 9. Vorticity contour plots for flow past the trailing edge of rectangular plates of different  $c/t$  ratios in the presence of transverse velocity perturbations applied at the natural ILEV/TEVS frequency for each plate. (a)  $c/t = 8$ ;  $\phi = 355^\circ$ , (b) 9;  $15^\circ$ , (c) 10;  $0^\circ$ .

as they are convected away from the model. However, vorticity from the L vortex remains identifiably separate from the T vortex with which it merges, even after the completion of one full shedding cycle from when the T vortex was shed. The cause of the asymmetry is not clear although it is noted that similar asymmetries were found in the predictions of Thompson *et al.* (1995).

The results for the two plates with  $c/t = 6$  and 7 show that transverse velocity perturbations applied at the frequency corresponding to the natural ILEV/TEVS shedding frequency for each plate resulted in vortex shedding being phase-locked to the perturbations. Transverse velocity perturbations were applied at frequencies corresponding to the natural ILEV/TEVS mode also for plates with  $c/t = 8$  and 10. The vortex shedding from the plate with  $c/t = 9$  could not be locked to the transverse perturbations at the frequency corresponding to ILEV/TEVS mode 2, this being the natural vortex-shedding frequency measured in the water tunnel (see discussion in §3.1). For this plate, perturbations were applied at a frequency corresponding to ILEV/TEVS mode 3 (the natural frequency measured by Nakamura *et al.* 1991). Figure 9 shows vorticity contour plots for these three different length plates, with

the phase of the perturbation cycle for each case indicated and selected to show the wake vortices in similar positions. For all three plates, the vortex shedding at both the leading and trailing edges was phase-locked to the perturbations.

As mentioned above, when leading-edge shedding is phase locked to the sinusoidal perturbation field, L vortices are shed at the same phase in the perturbation cycle regardless of  $c/t$  ratio. Depending on both  $c/t$  ratio and perturbation frequency, it can take several perturbation cycles for an L vortex to reach the trailing edge. The phase in the perturbation cycle at which an L vortex passes the trailing edge depends on both the  $c/t$  ratio and the perturbation frequency, as the convection velocity of vortices along the side of the plate is relatively independent of  $c/t$  ratio. For all five plate lengths tested (i.e. 6, 7, 8, 9 and 10), adjusting the frequency to equal that of the natural ILEV/TEVS mode results in a different spacing between adjacent L vortices on the sides of the plate. The result of this adjustment of spacing in all cases is that L vortices shed from the upper leading-edge corner pass the trailing edge when the phase of the perturbation cycle is approximately  $0^\circ$ . At this same phase, a clockwise rotating T vortex, formed from the reattached boundary layer ahead of the oncoming L vortex, sheds and subsequently merges with the L vortex in the near wake. What this demonstrates is that strong trailing-edge shedding occurs for different length plates when transverse velocity perturbations are applied at a frequency corresponding to a natural ILEV/TEVS mode. This corresponds to frequencies that resulted in maximum values of base suction in the wind-tunnel experiments (Mills *et al.* 2002).

### 3.3. Transverse velocity perturbations applied at non-ILEV/TEVS frequencies

The interference that vortices shed from the leading edge (L vortices) have on the vortex shedding at the trailing edge (T vortices) and its dependence on the phase in the perturbation cycle at which they arrive at the trailing edge was investigated further. PIV and flow visualization data were collected for transverse velocity perturbations applied at frequencies half-way between ILEV/TEVS modes for each plate (i.e.  $St_p = 0.6(n + 0.5)$ ).

Figure 10 shows PIV of a full cycle of vortex shedding in the flow with a plate of  $c/t = 7$  in the presence of a 6.5% velocity perturbation applied at a frequency of 0.75 Hz ( $St_p = 0.212$ ); this corresponds to an ILEV/TEVS mode of 2.5. It can be seen that L vortices are convected into the wake, where they interact to form an alternating vortex street. No T vortices are formed in this case because the clockwise rotating L vortex on the upper side of the plate adjacent to the trailing edge arrives at the trailing edge at a phase in the perturbation cycle of  $180^\circ$  and interferes with vortex shedding at the trailing edge. With the phase of the perturbation cycle equal to  $180^\circ$ , the perturbation velocity will increase in the downwards direction as the cycle continues, resulting in the reattached boundary-layer fluid adjacent to the lower trailing-edge corner being convected past the trailing edge and into the wake, without rolling up to form a T vortex.

If the phase of the perturbation cycle were  $0^\circ$  (i.e.  $180^\circ$  different), then the reattached boundary-layer fluid, containing the vorticity originally separating at the leading edge, adjacent to the trailing edge on the lower side of the plate in figure 10(c) would be in the correct position for an anticlockwise rotating T vortex to form. This is the case when the perturbation frequency is equal to a natural ILEV/TEVS frequency; this could be achieved by either changing the perturbation frequency or the  $c/t$  ratio.

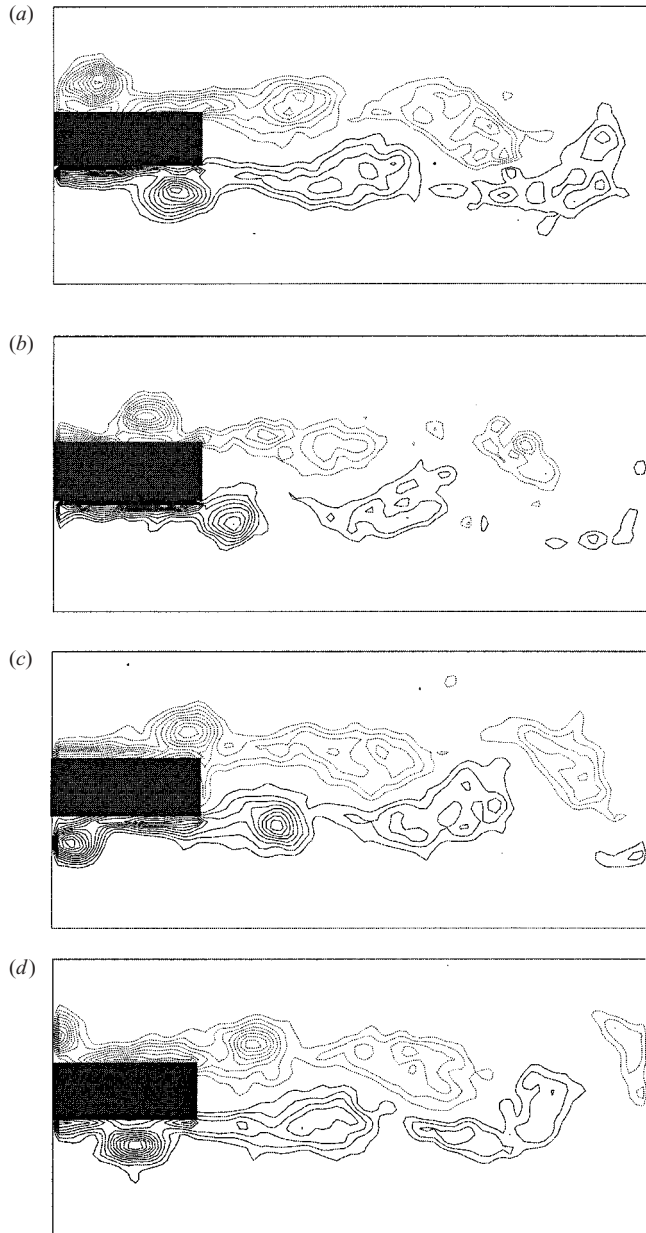


FIGURE 10. Vorticity contour plots for flow past the trailing edge of a rectangular plate with  $c/t = 7$ ,  $Re = 490$ , 5% velocity perturbation,  $St_p = 0.212$ . (a)  $\phi = 0^\circ$ , (b)  $90^\circ$ , (c)  $180^\circ$ , (d)  $285^\circ$ .

Note that the convection of L vortices of opposite sign into the wake, independent of whether trailing-edge shedding occurs, would explain why Parker & Welsh (1983) observed vortex shedding in the wake over the range  $0.05 < St_p < 0.25$ .

Compare the two PIV images from plates with  $c/t = 7$  in figures 8(c) and 10(c), both at a phase angle of  $180^\circ$  in the perturbation cycle, but with different perturbation frequencies. Clearly shown is how L vortices can interfere with the vortex shedding at

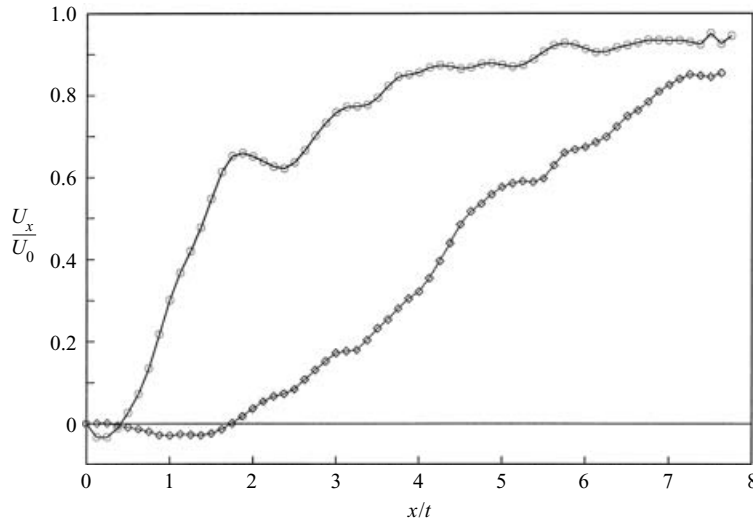


FIGURE 11. Variation of time-averaged  $U_x$  component of velocity with normalized distance from the trailing edge ( $x/t$ ) for two different perturbation frequencies.  $\circ$ ,  $St_p = 0.172$ ;  $\diamond$ , 0.212.

the trailing edge. The image in figure 8(c) has the perturbation frequency equal to the natural ILEV/TEVS mode 2 ( $St_p = 0.172$ ). It shows a strong anticlockwise rotating T vortex in the near wake, and the presence of reattached boundary-layer fluid adjacent to the upper trailing-edge corner which is about to be convected past the trailing edge to roll up and form a clockwise rotating T vortex. The other image, figure 10(c), is for a frequency corresponding to an ILEV/TEVS mode of 2.5 ( $St_p = 0.212$ ) and shows no T vortices being formed. Instead of reattached boundary-layer fluid being adjacent to the upper trailing-edge corner when the phase of the perturbation cycle is  $180^\circ$ , the fluid there is part of an L vortex that interferes with the formation of a T vortex. In the absence of trailing-edge vortex shedding, there is a larger region of stagnant fluid behind the trailing edge, corresponding to a greater vortex formation length.

Although the vortex formation length has not been measured directly here, figure 11 shows a comparison of the time-mean streamwise component of velocity,  $U_x$ , for the two cases ( $St_p = 0.172$  and 0.212) and how this varies with distance from the trailing edge ( $x/t$ ) (after averaging over four images taken  $90^\circ$  apart in the perturbation cycle and thus covering one shedding cycle). The region of reverse flow (negative  $U_x$ ) is seen to extend much further downstream when vortex shedding is suppressed ( $St_p = 0.212$ ).

Figure 11 and the vorticity contour plots shown in figures 8 and 10 show that when there is regular shedding of T vortices at the trailing edge, the vortex formation length is significantly reduced. Mills *et al.* (2002) showed that perturbations applied at the natural ILEV/TEVS frequency for the plate with  $c/t = 7$  of  $St_p = 0.172$  in the wind tunnel resulted in large negative base pressure coefficients,  $Cp_b$ , a consequence of the strong trailing-edge vortex shedding and correspondingly shorter vortex formation length that was observed in the water tunnel. A much smaller negative  $Cp_b$  was measured in the wind tunnel when  $St_p = 0.212$ , which is consistent with the results from the water tunnel that showed no trailing-edge vortex shedding and a correspondingly longer vortex formation length for perturbations applied at this frequency.

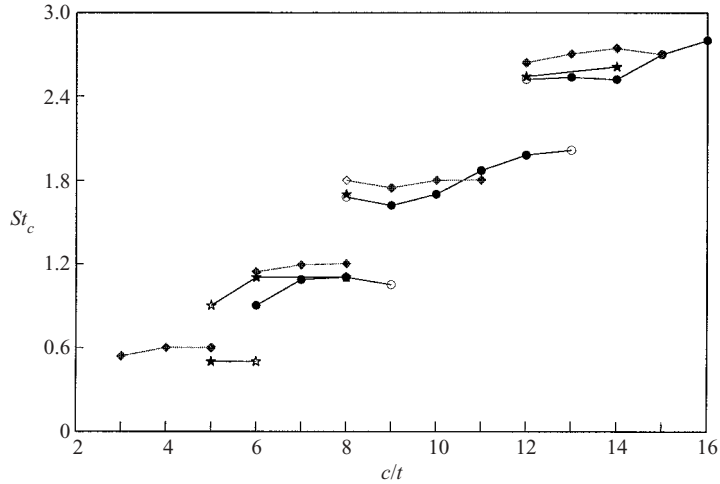


FIGURE 12. Vortex shedding  $St_c$  for elongated rectangular plates; ●,  $St_{p_c}$  (based on plate chord) corresponding to peaks in  $Cp_b$  data (4.5% perturbation level); ◆,  $St_c$  measured by Nakamura at  $Re = 1000$ ; ★,  $St_c$  measured by Stokes & Welsh (1986).

#### 3.4. Mechanism of frequency selection

Although the feedback route and/or nature of the perturbing pressure pulse directly controlling leading-edge shedding for the three independent experiments of Nakamura *et al.* (1991) (natural shedding), Stokes & Welsh (1986) (duct acoustic resonance) and this study (applied forcing) are different, the similarity in the  $St_c$  data shown in figure 12 for the three experiments is due to the dependency in each case on strong trailing-edge vortex-shedding, which in turn depends on the phase in the leading-edge vortex-shedding cycle at which L vortices pass the trailing edge, regardless of  $c/t$  ratio.

The results of the study by Mills *et al.* (2002) show that when the  $St_p$  at which peaks in base suction occur are multiplied by plate chord, they are similar to the  $St_c$  corresponding to the natural ILEV/TEVS frequencies. In turn, they are similar to the stepping of the frequencies at which maximum sound pressure levels of duct acoustic resonance occur when rectangular cylinders are placed in duct flows (Stokes & Welsh 1986). In the following, we discuss how the stepwise variation in figure 12 arises in the natural and forced cases.

We have shown that natural vortex shedding from rectangular plates at low  $Re$  is characterized by the ILEV/TEVS instability, where  $St_c = 0.6n$ . Figure 13 illustrates how vortex shedding is locked to the plate chord. Vortex shedding from the leading edge is periodic, and L vortices may take several shedding cycles to be convected past the trailing edge once shed from the leading-edge separation bubble. Since the leading-edge shedding responds to pressure pulses that are generated by T vortex shedding in between L vortices passing the trailing edge, L vortices always pass the trailing edge at the same phase in the leading-edge shedding cycle regardless of  $c/t$  ratio. Nakamura *et al.* (1991) showed that the convection velocity of L vortices along the sides of the plates is almost independent of the  $c/t$  ratio. Figure 13 also demonstrates how the frequency of vortex shedding varies with plate  $c/t$  ratio so that L vortices take an integer number of leading-edge shedding cycles to reach the trailing edge.

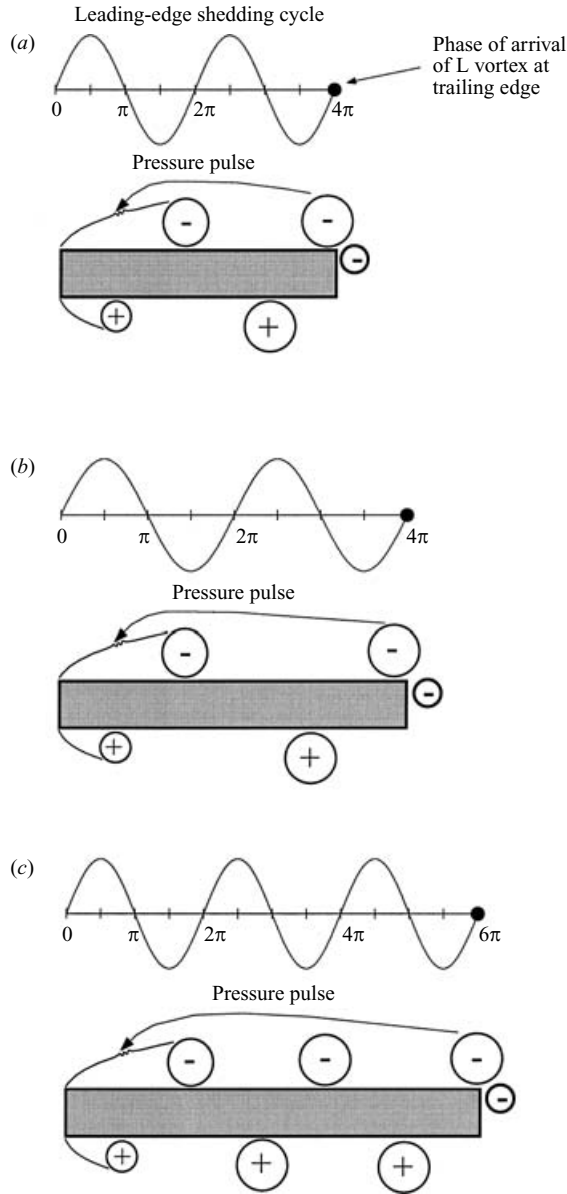


FIGURE 13. Illustration of ILEV/TEVS shedding mechanism, showing the effect on spacing between L vortices of changing plate  $c/t$  ratio. L vortices always pass the trailing edge at the same phase in the leading-edge shedding cycle regardless of  $c/t$  ratio. (a) ILEV/TEVS mode 2,  $c/t = 6$ ; (b) ILEV/TEVS mode 2,  $c/t = 7$ ; (c) ILEV/TEVS mode 3,  $c/t = 9$ .

It should be noted that the ILEV/TEVS instability is hydrodynamic in nature, meaning that in the low-Mach-number flows of interest, the feedback pressure pulses travel upstream to control the leading-edge shedding directly and almost instantaneously. Evidently, as  $Re$  is increased above 2000, increased turbulence breaks down or over-rides the feedback path, resulting in a loss of regular vortex shedding.

Peaks in base suction occur when strong trailing-edge shedding is excited by the transverse velocity perturbations generated by loudspeakers located on either

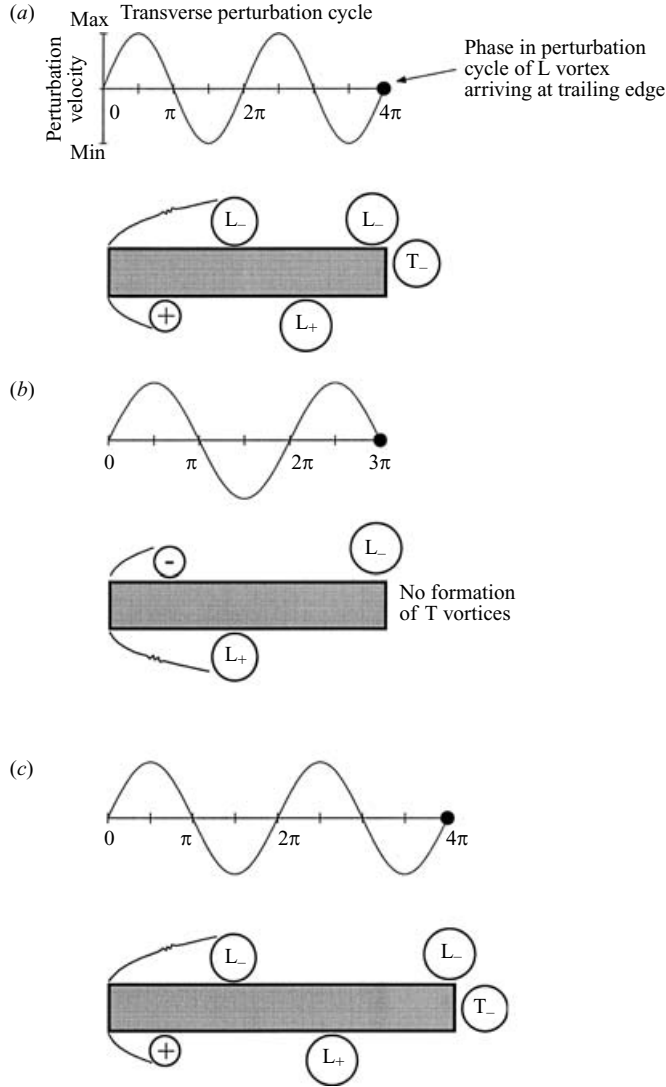


FIGURE 14. Illustration of shedding from rectangular plates in the presence of transverse velocity perturbations, showing the effect on trailing-edge shedding of changing the phase in the perturbation cycle that L vortices pass the trailing edge. Peaks in base suction occur when T vortices are shed, because L vortices always pass the trailing edge at the same phase in the acoustic resonance cycle regardless of  $c/t$  ratio. (a)  $c/t = 6$ ,  $St = 0.18$  ( $St_c = 1.2$ : equivalent to ILEV/TEVS mode 2). T vortices are formed since  $L_-$  vortices arrive at the trailing edge at  $0^\circ$  in the perturbation cycle. (b)  $c/t = 6$ ,  $St = 0.154$  ( $St_c = 0.9$ : equivalent to ILEV/TEVS mode 1.5). No T vortices are formed since  $L_-$  vortices arrive at the trailing edge at  $180^\circ$  in the perturbation cycle. (c)  $c/t = 8$ ,  $St = 0.154$  ( $St_c = 1.2$ : equivalent to ILEV/TEVS mode 2). T vortices are formed since  $L_-$  vortices arrive at the trailing edge at  $0^\circ$  in the perturbation cycle.

side of the rectangular plates (Mills *et al.* 2002). T vortices are shed when the perturbation frequency is equal to a natural, low  $Re$ , ILEV/TEVS frequency. L vortices are convected at a constant velocity independent of  $c/t$  ratio. Thus, the phase in the perturbation cycle at which they pass the trailing edge depends on both the perturbation frequency and the  $c/t$  ratio. This is illustrated in figure 14(a) where

perturbations applied at a natural ILEV/TEVS frequency for  $c/t = 6$  result in L vortices passing the upper trailing-edge corner at  $0^\circ$  in the perturbation cycle, thus allowing T vortices to form. Changing the perturbation frequency changes the number of cycles it takes for an L vortex to be convected to the trailing edge (figure 14*b*). The L vortex now passes the trailing edge at a phase in the perturbation cycle of  $180^\circ$ . At this phase, it interferes with trailing-edge shedding and no T vortices form. Figure 14(*c*) illustrates the effect of applying perturbations at the same frequency as in figure 14(*b*), but for a plate with a different  $c/t$  ratio. Now the L vortices take an extra half-cycle before they pass the trailing edge, meaning that they pass the trailing edge at  $0^\circ$  in the perturbation cycle. Thus, there is strong shedding of T vortices in figure 14(*c*), as in figure 14(*a*).

T vortices are shed when the perturbation frequency allows L vortices to pass the trailing edge at the same favourable phase in the perturbation cycle, for any  $c/t$  ratio. This occurs at the natural ILEV/TEVS frequencies, although in the forced case, the pressure pulses locking the leading-edge shedding are no longer provided by the trailing-edge shedding but rather by the applied forcing. For the resonant shedding in the duct observed by Stokes & Welsh (1986), leading-edge shedding is controlled by the transverse resonant duct acoustic mode perturbations (built up over many successive shedding cycles) and not by the direct feedback of individual pressure pulses from the trailing edge. At higher Reynolds number (greater than approximately 2000), where the self-sustained oscillations are no longer observed, locked shedding similar to the natural ILEV/TEVS case can still exist if forcing is applied by sound speakers or by an excited duct resonance mode.

#### 4. Conclusions

PIV measurements and flow visualization have shown that vortex shedding at the leading and trailing edges of rectangular cylinders can be simultaneously phase-locked to transverse velocity perturbations when the perturbation  $St_p$  is close to a natural ILEV/TEVS frequency. When this occurred, L vortices were found to always pass the trailing edge at the same phase in the perturbation cycle regardless of  $c/t$  ratio.

Applying perturbations at an  $St_p$  not equal to a natural ILEV/TEVS frequency results in phase-locked vortex shedding from the leading edge, and a near wake with a frequency equal to the perturbation frequency. This is consistent with the findings of Parker & Welsh (1983). However, vortex shedding at the trailing edge is either very weak or non-existent. PIV results and flow visualization showed trailing-edge vortices did not form because L vortices arrive at the trailing edge at a phase in the perturbation cycle when they interfere with trailing-edge shedding. T vortices are shed only when L vortices arrive at the trailing edge in a certain range of phase in the perturbation cycle, allowing the reattached boundary layer to roll up to form T vortices. The frequencies for which trailing-edge vortex shedding is most vigorous for different  $c/t$  ratios correspond to the natural ILEV/TEVS frequencies.

At  $Re = 10\,000$ , Stokes & Welsh (1986) showed that vortex shedding from rectangular plates located centrally in a duct could generate loud resonant sound at the duct  $\beta$ -mode (a transverse mode) resonant frequency. The  $St$  at which maximum sound pressure levels occurred for plates with different  $c/t$  ratios closely matched the 'ILEV' frequencies measured by Nakamura *et al.* (1991). Because of this, Nakamura *et al.* (1991) suggested that the vortex shedding observed by Stokes & Welsh (1986) was due to the 'ILEV' instability being excited by the resonant sound in the duct. Stokes & Welsh (1986) showed that leading-edge shedding was locked to the transverse

velocity perturbations associated with the resonant acoustic field in the duct, clearly a vortex shedding mechanism different to the ILEV/TEVS instability mechanism, which relies on pressure pulses generated by trailing-edge shedding being fed back upstream directly to the leading-edge shear layer to control leading-edge shedding. Peaks in base suction, and the concomitant pressure pulses feeding directly back to the leading edge in the natural shedding case or contributing over many cycles to a duct resonant acoustic mode, occur when trailing-edge shedding appears and is strong. Trailing-edge shedding in turn is dependent on  $L$  vortices passing the trailing edge at a favourable phase of the perturbation cycle, and thus of the leading-edge shedding cycle.

The common dependence on strong trailing-edge vortex shedding in each case is the reason for the similarity in the  $St$  vs.  $c/t$  relationship for the three seemingly different sets of experiments of Nakamura *et al.* (1991), Stokes & Welsh (1986) and the current study.

Dr Richard Mills acknowledges the support of an Australian Post Graduate Scholarship and use of the facilities at CSIRO Building, Construction and Engineering, Melbourne.

#### REFERENCES

- ADRIAN, R. J. 1991 Particle-imaging techniques for experimental fluid mechanics. *Annu. Rev. Fluid Mech.* **23**, 261–304.
- GRANT, I. 1997 Particle image velocimetry: a review. *Proc. IMechE* **211** Part C, 55–76.
- HO, C. M. & HUANG, L. S. 1982 Subharmonics and vortex merging in mixing layers. *J. Fluid Mech.* **119**, 443–473.
- HO, C. M. & NOSSEIR, N. S. 1981 Dynamics of an impinging jet. Part 1. The feedback phenomenon. *J. Fluid Mech.* **105**, 119–142.
- HOURLIGAN, K., MILLS, R. H., THOMPSON, M. C., SHERIDAN, J., DILIN, P. & WELSH, M. C. 1993a Base pressure coefficients for flows around rectangular plates. *J. Wind Engng Indust. Aerodyn.* **49**, 311–318.
- HOURLIGAN, K., THOMPSON, M. C., BROCHER, E. & ANDRIANANTOANDRO, A. 1993b Coupling of vortex shedding with the fundamental resonant mode of a resonator tube. *Noise Control Engng J.* **41**, 331–337.
- HOURLIGAN, K., THOMPSON, M. C. & TAN, B. T. 2001 Self-sustained oscillations in flows around long blunt plates. *J. Fluids Struct.* **15**, 387–398.
- HOURLIGAN, K., THOMPSON, M. C., WELSH, M. C. & BROCHER, E. 1992 Acoustic sources in a tripped flow past a resonator tube. *AIAA J.* **30**, 1484–1491.
- HOURLIGAN, K., WELSH, M. C., THOMPSON, M. C. & STOKES, A. N. 1990 Aerodynamic sources of acoustic resonance in a duct with baffles. *J. Fluids Struct.* **4**, 345–370.
- HOWE, M. S. 1975 Contributions to the theory of aerodynamic sound, with applications to excess jet noise and the theory of the flute. *J. Fluid Mech.* **71**, 625–673.
- MILLS, R., SHERIDAN, J. & HOURLIGAN, K. 2002 Response of base suction and vortex shedding from rectangular prisms to transverse forcing. *J. Fluid Mech.* **461**, 25–49.
- MILLS, R., SHERIDAN, J., HOURLIGAN, K. & WELSH, M. C. 1995 The mechanism controlling vortex shedding from rectangular bluff bodies. *Proc. 12th Australasian Fluid Mech. Conf. December 10–15, Sydney, Australia*, pp. 227–230.
- NAKAMURA, Y. 1996 Vortex shedding from bluff bodies with splitter plates. *J. Fluids Struct.* **10**, 147–158.
- NAKAMURA, Y. & NAKASHIMA, M. 1986 Vortex excitation of prisms with elongated rectangular, H and T cross-sections. *J. Fluid Mech.* **163**, 149–169.
- NAKAMURA, Y., OHYA, Y. & TSURUTA, H. 1991 Experiments on vortex shedding from flat plates with square leading and trailing edges. *J. Fluid Mech.* **222**, 437–447.

- NAUDASCHER, E. & ROCKWELL, D. 1994 *Flow Induced Vibrations – An Engineering Guide*. A. A. Balkema.
- NGUYEN, D. T. 1990 Gate vibrations due to unstable flow separation. *J. Hydraul. Engng ASCE* **116**, 342–361.
- OHYA, Y., NAKAMURA, Y., OZONO, S., TSURUTA, H. & NAKAYAMA, R. 1992 A numerical study of vortex shedding from flat plates. *J. Fluid Mech.* **236**, 445–460.
- PARKER, R. 1967 Resonance in wake shedding from parallel plates: calculation of resonant frequencies. *J. Sound Vib.* **5**, 332–343.
- PARKER, R. 1997 Aeroacoustics. *Intl J. Fluid Dyn.* (<http://elecpress.monash.edu.au/ijfd>), **1**, Article 1.
- PARKER, R. & WELSH, M. C. 1983 Effects of sound on flow separation from blunt flat plates. *Intl J. Heat Fluid Flow* **4**, 113–128.
- PERRY, A. E., CHONG, M. S. & LIM, T. T. 1982 The vortex shedding process behind two-dimensional bluff bodies. *J. Fluid Mech.* **116**, 77–90.
- ROCKWELL, D. & NAUDASCHER, E. 1978 Review – self sustaining oscillations of flow past cavities. *Trans. ASME J. Fluids Engng* **100**, 152–165.
- STOKES, A. N. & WELSH, M. C. 1986 Flow–resonant sound interaction in a duct containing a plate. Part II: Square leading edge. *J. Sound Vib.* **104**, 55–73.
- STONEMAN, S. A. T., HOURIGAN, K., STOKES, A. N. & WELSH, M. C. 1988 Resonant sound caused by flow past two plates in tandem in a duct. *J. Fluid Mech.* **192**, 455–484.
- TAN, B. T., THOMPSON, M. C. & HOURIGAN, K. 1998 Flow around long rectangular plates under cross flow perturbations. *Intl J. Fluid Dyn.* (<http://elecpress.monash.edu.au/ijfd>), **2**, Article 1.
- THOMPSON, M. C., MILLS, R., SHERIDAN, J. & HOURIGAN, K. 1995 Simulation of acoustically forced flows around long rectangular plates. *Proc. 12th Australasian Fluid Mech. Conf. December 10–15, Sydney*, pp. 513–516.
- WU, J. 1994 Three dimensional vortex structures in the wake of a bluff body. PhD thesis, Monash University, Melbourne, Australia.
- WU, J., SHERIDAN, J., SORIA, J., WELSH, M. C. & HOURIGAN, K. 1993 Experimental investigation of vortex shedding from a plate: effect of external velocity perturbation. *J. Wind Engng Indust. Aerodyn.* **49**, 401–410.